Applied Ocean Research 120 (2022) 103053

Contents lists available at ScienceDirect

Applied Ocean Research

journal homepage: www.elsevier.com/locate/apor

Towards a general design evaluation tool: The development and validation of a VPP for autonomous sailing monohulls

Yang An [a,b,c], Jiancheng Yu [a,b,*], Feng Hu [a,b], Zhenyu Wang [a,b]

[a] State Key Laboratory of Robotics, Shenyang Institute of Automation, Chinese Academy of Sciences, Shenyang 110016, China
[b] Institutes for Robotics and Intelligent Manufacturing, Chinese Academy of Sciences, Shenyang 110169, China
[c] University of Chinese Academy of Sciences, Beijing 100049, China

ARTICLE INFO

Keywords:
Autonomous sailboat
Velocity prediction program
General design
Optimization

ABSTRACT

Sailing speed performance is a crucial indicator that significantly affects the trafficability, efficiency, and tracking capability of autonomous sailing monohulls during marine science missions. Considering that the design of the hull and keel of an autonomous sailing monohull is usually a task-orientated and creative process, estimating speed performance by traditional velocity prediction programs (VPPs) based on empirical formulas and gradient solvers will lead to errors. This paper proposes a generalized VPP for helping designers assess the speed performance of their autonomous sailing monohulls. We designed an enhanced genetic algorithm (GA) solver to help the VPP converge quickly without a priori performance estimation. Furthermore, we propose an innovative neighbourhood information-based optimization (NIBO) strategy to accelerate and refine the solutions using adjacent states (external conditions with the same true wind speed (TWS) or true wind angle (TWA)) instead of culminating prediction by solving each state independently. We provide an application of the proposed VPP on our prototype as an example. Moreover, the numerical and experimental results show that the proposed VPP can serve as a practical design evaluation tool, especially in the early stages of design.

1. Introduction

Single-hulled autonomous sailboats (namely, autonomous sailing monohulls) exhibit good endurance and adaptability to heavy seas. Therefore, they are considered a promising platform for the growing demand of long-term marine science activities (Silva et al., 2019). To date, dozens of distinctive autonomous sailing monohulls have been designed and are playing roles in multitudinous tasks (Neal, 2006; Augenstein et al., 2016; Baker et al., 2015; Meinig et al., 2015; De Robertis et al., 2019; Klinck et al., 2016). For autonomous sailing monohulls, speed performance is an important design consideration. Sailing speed reflects trafficability in strong current regions, affects the efficiency in area coverage tasks, and determines whether a specific target can be tracked (An et al., 2021). The speed performance of autonomous sailing monohulls is strongly coupled with the external environment (wind direction and speed) and determined by the general design—size matching amongst subsystems (sail, keel, hull, etc.). It cannot be characterized by a single value (such as the "average speed") and is impossible to be intuitively evaluated by one of the individual subsystems (Guelfi and Canepa, 2013). For the latter, an example can make this concept easier to understand: a narrower hull always indicates less resistance. However, the poor overturning resistance it provides increases the likelihood of being matched with a smaller sail to ensure that the platform does not overturn in a gale, which results in less driving force. Thus, the impact of a narrower hull on speed performance is still not intuitive. Therefore, the evaluation mechanism of speed performance is essential for designing and comparing autonomous sailing monohulls.

In crewed sailing, designers adopted velocity prediction programs (VPPs) to comprehensively evaluate the speed performance of a specific general design. As Fig. 1 shows, VPPs take a particular design and are given external conditions (true wind speeds and angles) as inputs. Then, multiple degrees of freedom (DOF) equations of aero- and hydrodynamics on subsystems are solved. If subsystem models are accurate, computing the maximum speed when faced with the given external conditions is feasible. Typically, VPPs provide polar curves that depict the optimal action vectors (of the sail and rudder) and the corresponding state vectors (speed and attitudes) to each given external condition (de jong et al., 2008; Graf and Bohm, 2005; Kerwin, 1975; ORC VPP, 2020). Nevertheless, few designers introduced the VPP to autonomous sailing monohull design. Briere (2008) formulates a control law by a program

* Corresponding author.
E-mail addresses: anyang@sia.cn (Y. An), yjc@sia.cn (J. Yu).

https://doi.org/10.1016/j.apor.2022.103053
Received 3 June 2021; Received in revised form 8 December 2021; Accepted 6 January 2022
Available online 12 January 2022

Nomenclature and abbreviations

A_L	lateral area above the waterline
AR	aspect ratio of components
A_T	transverse area above the waterline
Boa	overall beam
Bwl	waterline beam
c	mean chord of a specific component
C_{A2B}	conversion matrix between reference frames A and B
C_D	resistance coefficient of a resistance component
CE	centre of effort of the sail
CER	centre of effort of the rudder
CG	centre of gravity
C_L	lift coefficient of a specific component
CLR	centre of hydrodynamic force acting on the hull and keel
$c_{r\ ex}$	root chord of the extended keel
c_{tip}	tip chord of the extended keel
D	drag of a specified component
D_c	moulded depth of the canoe body
F_{lat_A}	lateral force generated by component A in the hull-fixed reference frame
F_{lon_A}	longitudinal force generated by component A in the hull-fixed reference frame
Fr	Froude number
F_{x_A}	driving force generated by component A in the inertial reference frame
F_{y_A}	lateral force generated by component A in the inertial reference frame
g	acceleration of gravity
L	lift on a specified component
l	span of a specified component
L_{oa}	overall length
L_{pp}	length between perpendiculars
L_{wl}	waterline length
$M_{\_A}$	overturning moment generated by component A
R_A	resistance components in the DSYHS model
Re	Reynolds number
S	lateral area of a specific component
t	mean thickness of a specific component
T	total draft with keel
Tc	draft of canoe body
V	inflow velocity of a specified component
VCG	vertical position of CG (below deck)
v	velocity projection vector of a specified component
v_s	sailboat velocity
v_t, TWS	true wind velocity
x_A	longitudinal distance from reference point A to CG
z_A	vertical distance from reference point A to CG
α	attack angle of a specified component
β_t, TWA	true wind angle
β_s	sail angle
β_r	rudder angle
Δ	total displacement
θ	heel angle
λ	yaw angle
ν	fluid kinematic viscosity
Λ	sweepback angle
ρ	density of air or water
φ	trim (pitch) angle

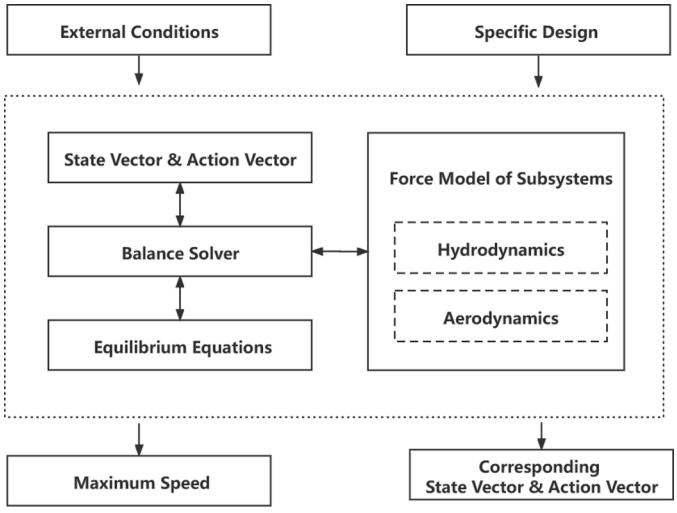

Fig. 1. The framework of the VPP.

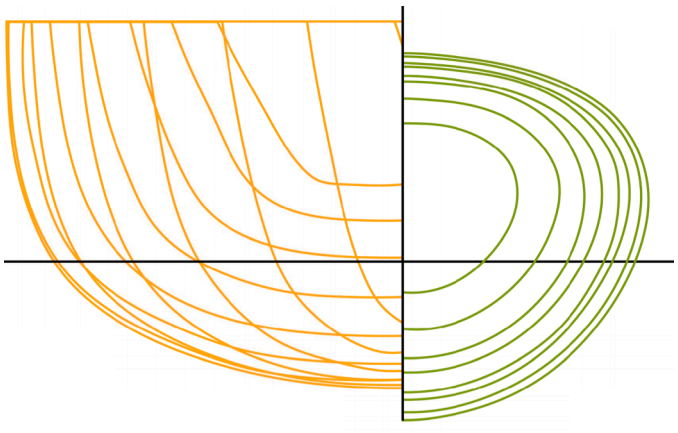

Fig. 2. Parent hull forms of the DSYHS (Keuning and Sonnenberg, 1998) V.S. Hull of A-TIRMA G2 (Domínguez-Brito et al., 2016).

with simplified models of the hull and sail. Rynne and von Ellenrieder (2010) implemented VPP based on the Delft systematic yacht hull series (DSYHS) formula (Keuning and Sonnenberg, 1998) and Xfoil code to optimize the design of the self-trimming wingsail of 'Maribot Vane.' Miller et al. (2018) compared the performances of a Viking-style wing sail and a traditional soft sail through 'PCSail,' a VPP based on DSYHS and gradient-based solvers, developed by Martin and Beck (2001).

However, none of the existing VPPs can serve as a generalized evaluation tool for autonomous sailing monohulls. First, most existing VPPs model the hydrodynamics of hulls and keels by empirical formulas (such as DSYHS (Keuning and Sonnenberg, 1998)). Compared to crewed sailboats, hull and keel designs of autonomous sailing monohulls may be task-scenario orientated (in terms of the arrangement of scientific loads, etc.) and can differ significantly from those 'standard' designs (Fig. 2). Errors in hull and keel hydrodynamics will strongly degrade the accuracy of VPP (Lasher et al., 2003; Gormand, 2015). Second, most existing VPPs balance aero- and hydrodynamics using initial value-sensitive gradient-based solvers. This approach is suitable for predicting the speed performance of crewed sailboats classified by 'classes,' whose high-quality performance estimation can be obtained from considerable amounts of regatta data. However, for autonomous sailing monohulls,

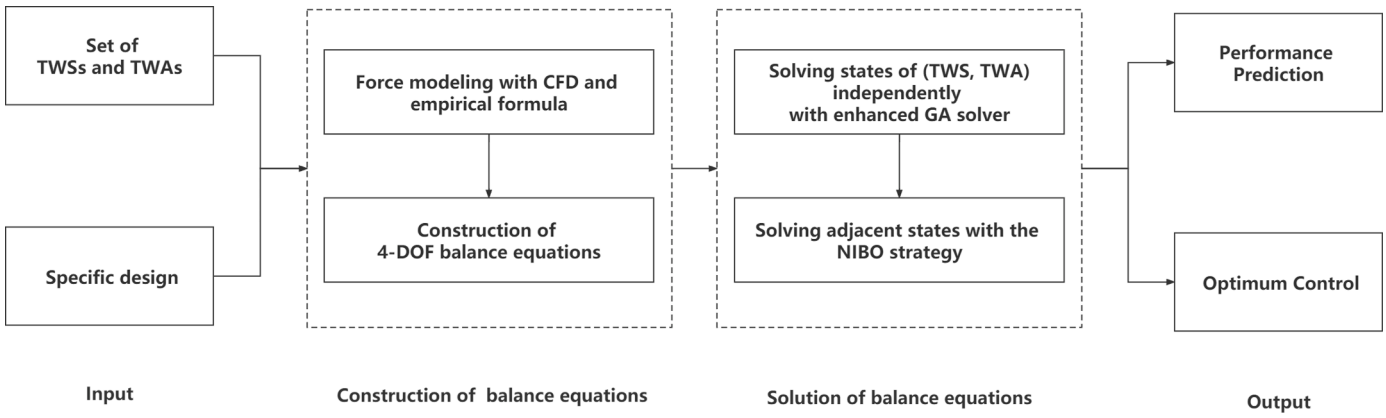

Fig. 3. The schematic of the proposed VPP.

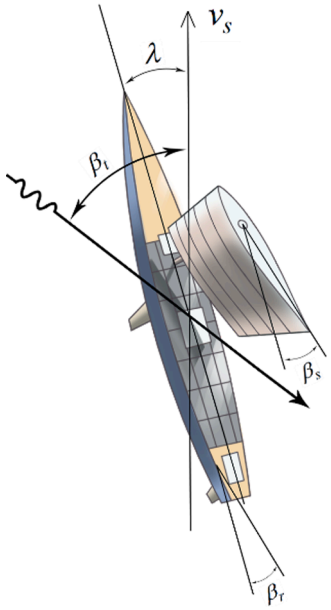

Fig. 4. Definition of a state under specific external conditions.

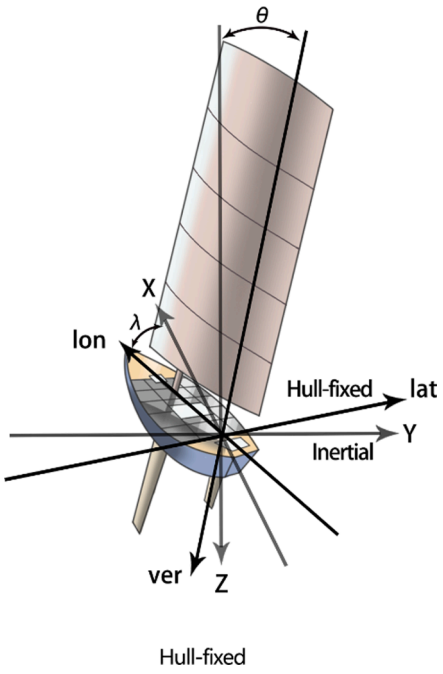

Fig. 5. Reference frames.

designers may struggle to obtain even a rough performance estimation at the design stage, which will seriously weaken the prediction ability of VPPs.

Therefore, we aim to propose a generalized VPP. With appropriate hydrodynamic and aerodynamic models from any source (especially from accurate computational fluid dynamics (CFD) simulations), the VPP can help designers assess the speed performance of their autonomous sailing monohulls. Considering the difficulty of obtaining high-quality performance estimations, we designed an enhanced genetic algorithm (GA) solver to help VPPs converge quickly. Furthermore, we propose an innovative neighbourhood information-based optimization (NIBO) strategy to accelerate and refine the solutions using adjacent states (external conditions with the same true wind speed (TWS) or true wind angle (TWA)) instead of culminating prediction by solving each state independently. Numerical simulations and sea trials prove the credibility and effectiveness of the proposed method and the VPP. We believe that the proposed VPP can serve as a powerful tool for autonomous sailing monohull designers. In this paper, the proposed VPP is detailed in Section 2; numerical simulations and sea trials are reported and discussed in Section 3. In Section 4, some conclusions are presented.

2. A VPP for autonomous sailing monohulls

The schematic of the proposed VPP is shown in Fig. 3. In the proposed VPP, the aerodynamic model of the sail and hydrodynamic model of the hull and keel can be obtained from appropriate sources. The balance equations of hydrodynamics and aerodynamics under given external conditions are constructed by coordinate transformation. 4-DOF balance equations (pitch and heave balance are neglected) are adopted to balance complexity and precision due to the small thrust-to-weight ratio and the massive longitudinal moment of inertia of autonomous sailing monohulls. A GA solver with an end-place enhancement module is designed to obtain the performance prediction without prior estimation. In addition, an innovative NIBO strategy is proposed to accelerate and refine the solution of such a high-dimensional nonconvex problem. The NIBO strategy makes use of natural continuity to provide information for the solution of adjacent states (states with the same TWS of TWA).

2.1. Construction of balance equations

As Fig. 4 shows, the state under specific external conditions (TWS v_t

Table 1
Transformation matrices between subsystems.

From	To	Rotation matrix C_{A2B}
Flow direction	Inertial	$C_{v2i} = E_{yaw}(\pi)$
True wind direction	Inertial	$C_{tw2i} = E_{yaw}(\pi + \beta_t)$
Inertial	Hull-fixed	$C_{i2h} = E_{yaw}(\lambda) \cdot E_{roll}(\theta)$
Hull-fixed	Sail chord	$C_{h2s} = E_{yaw}(\beta_s)$
Hull-fixed	Rudder chord	$C_{h2r} = E_{yaw}(\beta_r)$

and TWA β_t) consists of speed (v_s), attitude (heeling angle θ, yaw angle λ), and a control vector (sail trim β_s, rudder angle β_r). Two right-handed reference frames (Fig. 5) are defined with the centre of gravity (CG) for a clear description. The first is a hull-fixed frame denoted by subscripts *lon*, *lat*, and *ver* in which the x-direction lies along the longitudinal axis from the stern to the bow. The second is the inertial frame aligned with the direction of v_s, water surface, and gravity, denoted by the subscripts *X*, *Y*, *Z*, respectively. Transformation matrices between frames are given in Table 1.

Where

$$E_{yaw}(\lambda) = \begin{bmatrix} cos\lambda & -sin\lambda & 0 \\ sin\lambda & cos\lambda & 0 \\ 0 & 0 & 1 \end{bmatrix}, E_{pitch}(\varphi) = \begin{bmatrix} cos\varphi & 0 & sin\varphi \\ 0 & 1 & 0 \\ -sin\varphi & 0 & cos\varphi \end{bmatrix}, E_{roll}(\theta) = \begin{bmatrix} 1 & 0 & 0 \\ 0 & cos\theta & -sin\theta \\ 0 & sin\theta & cos\theta \end{bmatrix} \quad (1)$$

2.1.1. Modelling of hydrodynamics and aerodynamics

The prediction accuracy of VPP is strongly dependant on the accuracy of the hydro- and aerodynamic model of subsystems (Lasher et al., 2003; Gormand, 2015). Therefore, although the proposed VPP can be compatible with hydro- and aerodynamic models from any source, we still recommend modelling hulls and keels with CFD simulations, as they may be very different from the "standard" designs (Fig. 2).

The hydrodynamic force of the hull and keel can be obtained by the model $f(hull\ line, v_s, \theta, \lambda)$as Eq. (2).

$$\left[F_{x\_hk}, F_{y\_hk}\right] = f(hull\ line, v_s, \theta, \lambda) \quad (2)$$

Thus, the force in a hull-fixed frame F_{lon_hk} and F_{lat_hk} can be easily obtained from the conversion matrix C_{i2h} as Eq. (3).

$$\left[F_{lon\_hk}, F_{lat\_hk}, 0\right] = \left[F_{x\_hk}, F_{y\_hk}, 0\right] \cdot C_{i2h} \quad (3)$$

The rudders of autonomous sailing monohulls are generally similar in shape to "standard" rudders. To reduce the dimension of the matrix to be filled in by CFD simulation, empirical formulas are recommended to obtain the hydrodynamic force of the rudder. Both the lift and drag of the rudder act on the centre of effort of the rudder (CER). Due to the interference of the keel, the inflow velocity of the rudder is considered to be $0.95 \cdot v_s$[22] as Eq. (4). Eq. (5) can be used to calculate the inflow speed since the heave motion is ignored. Moreover, the attack angle of rudder α_r needs to be corrected by the downwash angle, as described in Eq. (6), where a_0 can be found in the study by Keuning et al. (2006). The lift can be calculated by Eq. (7), in which the lift coefficient slope can be determined by the formula by Whicker and Fehlner (1958) as Eqs. (8,9).

$$v_r = 0.95 \cdot v_s \cdot C_{v2r}. \quad (4)$$

$$V_r = \| \left(v_{rx}, v_{ry}, 0\right) \| \quad (5)$$

$$\alpha_r = tan^{-1}\left(\frac{v_{ry}}{v_{rx}}\right) - a_0 \cdot \sqrt{\frac{\frac{\partial C_{Lek}}{\partial \alpha_k} \cdot \alpha_k}{2 \cdot AR_{ek}}} \quad (6)$$

$$L = \frac{1}{2} \cdot \rho \cdot V^2 \cdot S \cdot \frac{\partial C_{Ler}}{\partial \alpha_r} \cdot \alpha_r \quad (7)$$

$$\frac{\partial C_{Ler}}{\partial \alpha_r} = \frac{5.7 \cdot AR_{er}}{1.8 + \cos\Lambda_i \sqrt{\frac{AR_{er}^2}{\cos^4 \Lambda_i} + 4}} \quad (8)$$

$$AR_{er} = 2 \cdot AR_r \quad (9)$$

The parameters of the keel can be obtained by Eqs. (10)–(12), and the effective aspect ratio of the keel is estimated by the extended keel method (Gerritsma, 1968).

$$v_k = v_s \cdot C_{v2h} \quad (10)$$

$$\alpha_k = tan^{-1}\left(\frac{v_{ky}}{v_{kx}}\right) \quad (11)$$

$$AR_{ek} = \frac{2 \cdot (l_k + T_c)}{\left(\frac{c_{r\_ex} + c_{tip}}{2}\right)} \quad (12)$$

The resistance produced by the rudder includes the induced resistance and profile resistance as Eqs. (13–15). The induced resistance coefficient is proportional to the square of the effective lift coefficient (Abbott and Von Doenhoff, 2012). The profile resistance coefficient can be obtained by the International Towing Tank Conference (ITTC) 1957 formula and the form factor.

$$D = \frac{1}{2} \cdot \rho \cdot V^2 \cdot S \cdot \left(\frac{\left(\frac{\partial C_{L\varepsilon}}{\partial \alpha} \cdot \alpha\right)^2}{\pi \cdot AR_e} + 2 \cdot \frac{0.075}{(\log(Re) - 2)^2} \cdot \left(1 + 2 \cdot \frac{t}{c} + 60 \cdot \left(\frac{t}{c}\right)^4\right) \right) \quad (13)$$

The projection of the force on the rudder in the inertial frame, F_{x_r} and F_{x_r}, and the hull-fixed reference frame, $F_{lon_r}$and F_{lat_r}, can be obtained by

$$\left[F_{x\_r}, F_{y\_r}, 0\right] = \left[-D, -L \cdot sign(\alpha), 0\right] \cdot E_{yaw}(-\alpha) \cdot C_{r2i} \quad (14)$$

$$\left[F_{lon\_r}, F_{lat\_r}, 0\right] = \left[-D, -L \cdot sign(\alpha), 0\right] \cdot E_{yaw}(-\alpha) \cdot C_{r2h} \quad (15)$$

For a sail, whether a soft sail or a wing sail, the force model is generally in the form of a drag coefficient $f_D(profile, \alpha, Re, AR)$and a lift coefficient$f_L(profile, \alpha, Re, AR)$. The only difference is that the wing sail's control quantity is the turning angle, while*flat* , *reef* , and *twist* are indicated for a soft sail. The aerodynamic model of soft sails can be obtained from empirical models such as the Jackson model or the Fossati model Kerwin, 1975; Fossati et al., 2006; Jackson, 1996; Jackson, 2001). We prefer to use CFD simulations to model the aerodynamics of the wingsail, as the full angle of attack data is required for small aspect ratio airfoils. The force acts on the centre of effort (CE), located at 25% of the chord length from the leading edge. The force components can be written as follows: The projection of the true wind vector on the sail *v* can be calculated according to Eq. (16), regardless of the heave motion, and the inflow velocity *V* can be expressed by Eq. (17). The angle of

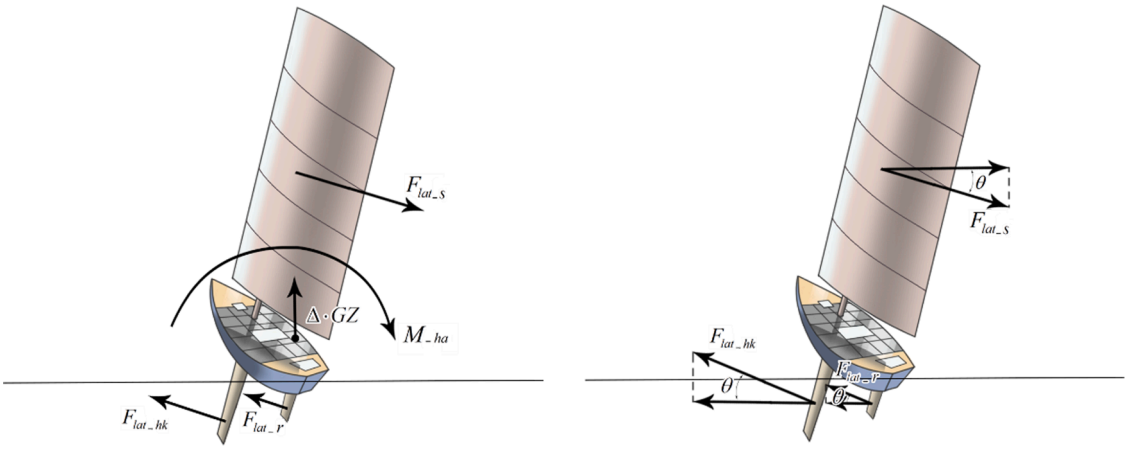

Fig. 6. Schematic diagrams of roll and yaw balance.

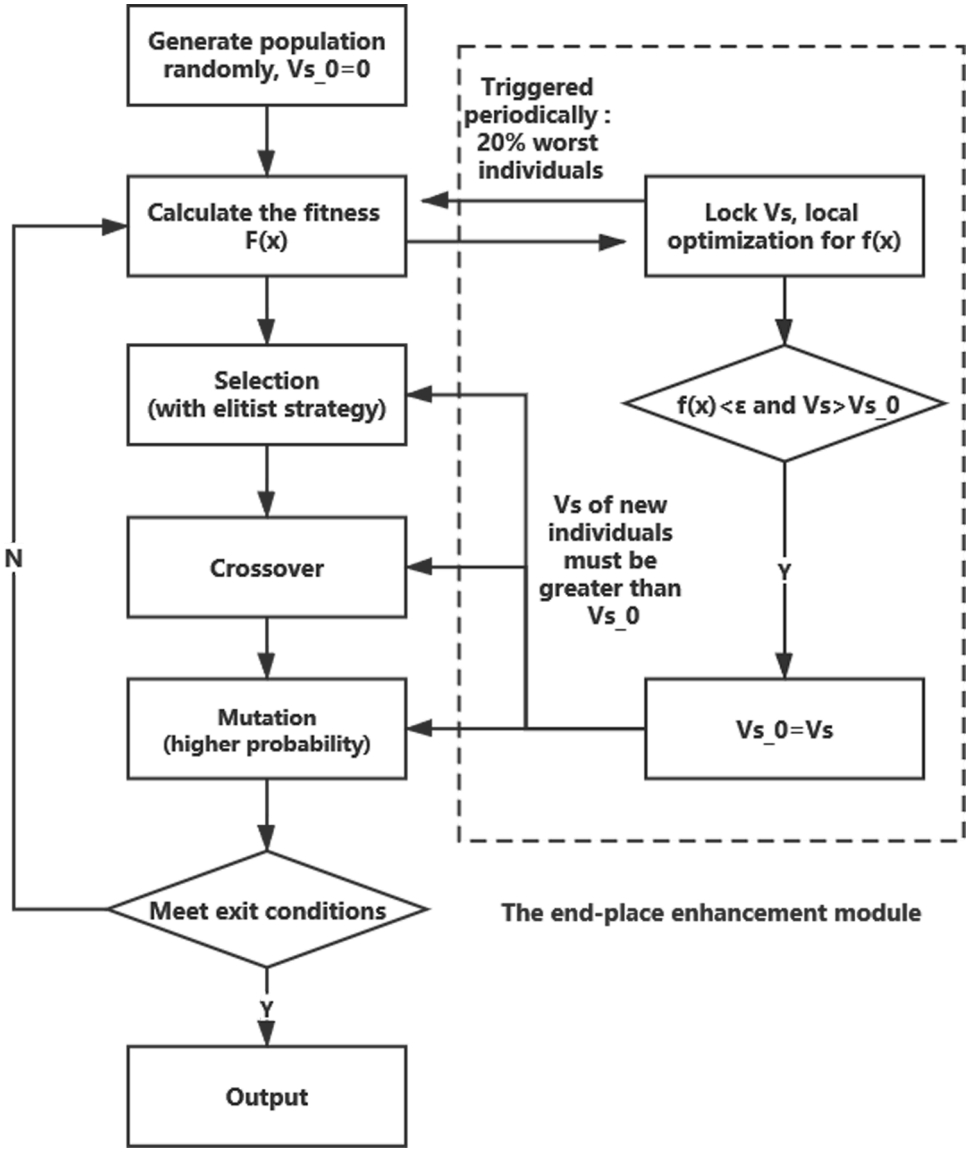

Fig. 7. Schematic of the end-place enhancement GA solver.

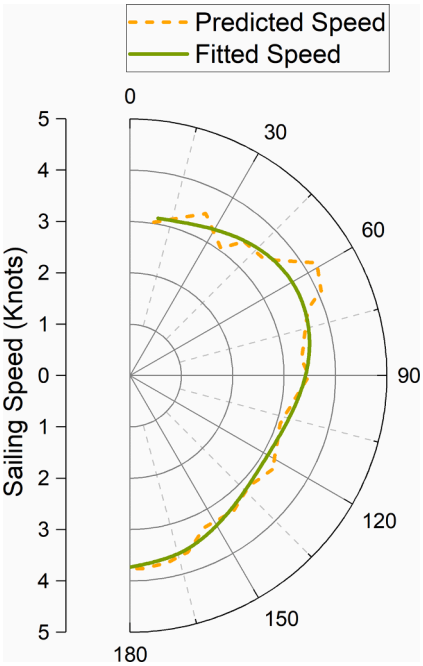

Fig. 8. Moving average implementation to smooth fluctuations of VPP predicted results (Clark, 2014).

attack αcan be calculated by Eq. (18). The lift and drag can be determined by Eqs. (19) and ((20), respectively.

$$v = v_t \cdot C_{tw2s} + v_s \cdot C_{v2s} \tag{16}$$

$$V = \| \ (v_x, v_y, 0) \ \| \tag{17}$$

$$\alpha = tan^{-1}\left(\frac{v_y}{v_x}\right) \tag{18}$$

$$L = \frac{1}{2}\cdot\rho\cdot V^2 \cdot S \cdot f_L(profile, \alpha, Re, AR) \tag{19}$$

$$D = \frac{1}{2}\cdot\rho\cdot V^2 \cdot S \cdot f_D(profile, \alpha, Re, AR) \tag{20}$$

The projection of force on the sail in the inertial reference frame, F_{x_s} and F_{y_s}, and in the hull-fixed reference frame, $F_{lon_s}$and F_{lat_s}, can be calculated as Eqs. (21,22)

$$[F_{x\_s}, F_{y\_s}, 0] = [-D, -L\cdot sign(\alpha), 0]\cdot E_{yaw}(-\alpha)\cdot C_{s2i} \tag{21}$$

$$[F_{lon\_s}, F_{lat\_s}, 0] = [-D, -L\cdot sign(\alpha), 0]\cdot E_{yaw}(-\alpha)\cdot C_{s2h} \tag{22}$$

For aerodynamic forces on the hull, only the force acting on the hull is considered since the mast is wrapped in the wing sail. The hull can be approximated as a profile with a small aspect ratio (AR) and often works in poststall conditions. Hence, the lift of the hull can be neglected. Coefficients and formulas that can be used to approximate the aerodynamic force can be found in the work by Fujiwara et al. (1998) as Eqs. (23–26).

$$F_{lon\_ha} = \frac{1}{2}\cdot\rho\cdot V^2 \cdot A_T \cdot C_{lon\_ha} \tag{23}$$

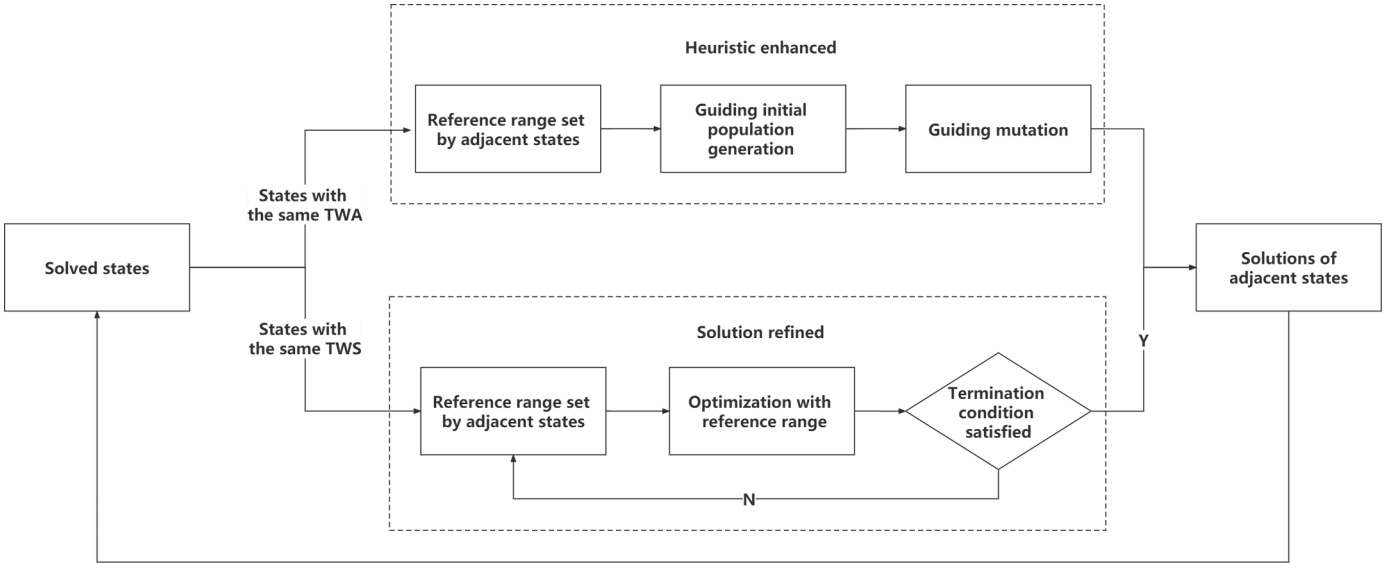

Fig. 9. The NIBO strategy.

Table 2
Design variables of prototype components.

Hull						Keel					
Δ	155	kgf	*VCG*	−265	mm	Profile			NACA 63,015		
L_{oa}	3420	mm	B_{oa}	1175	mm	c_{max}	296	mm	c_{min}	150	mm
L_{wl}	3250	mm	B_{wl}	965	mm	Λ	44	°	*l*	714	mm
D_c	410	mm	T_c	105	mm						
Sail						Rudder					
Profile			NACA 0012			Profile			NACA 0012		
c_{max}	745	mm	c_{min}	745	mm	c_{max}	140	mm	c_{min}	100	mm
Λ	0	°	*l*	1600	mm	Λ	0	°	*l*	320	mm

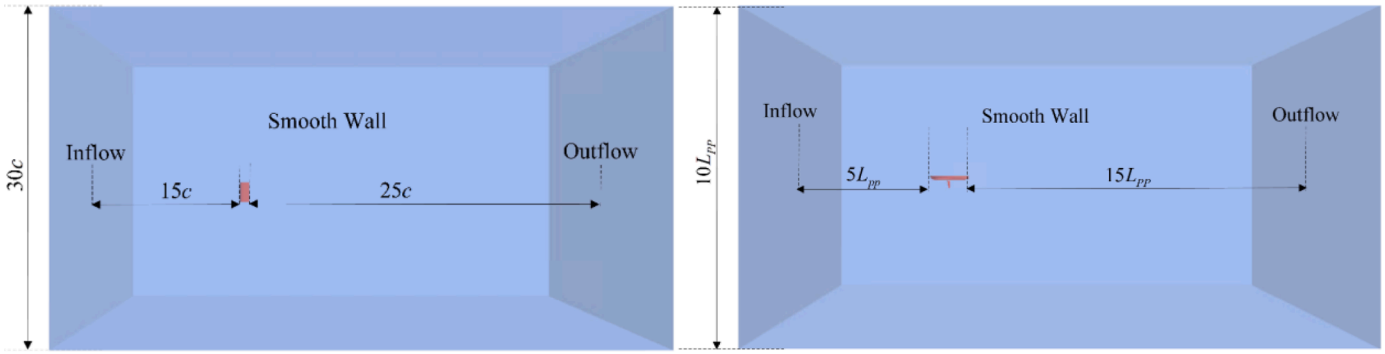

Fig. 10. Setup of the computational domain.

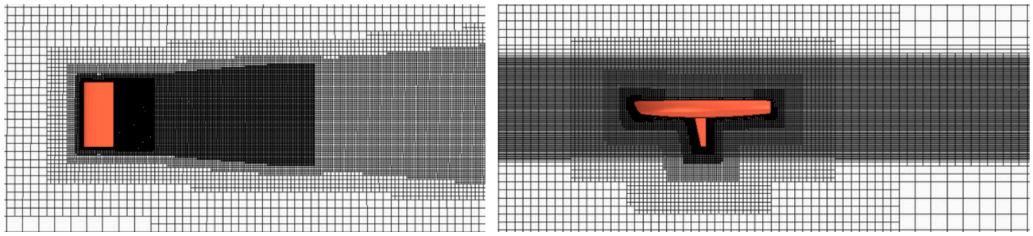

Fig. 11. Mesh settings.

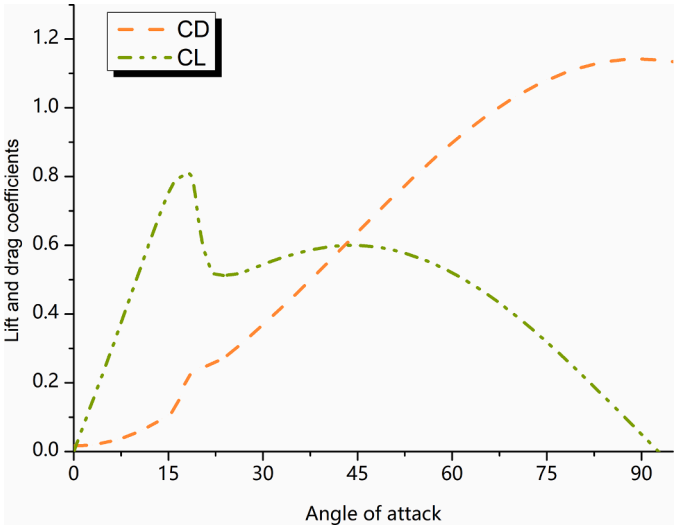

Fig. 12. CL and CD curves of the sail.

$$F_{lat\_ha} = \frac{1}{2}\cdot\rho\cdot V^2\cdot A_L\cdot C_{lat\_ha} \tag{24}$$

$$M_{\_ha} = \frac{1}{2}\cdot\rho\cdot V^2\cdot C_{M\_ha}\cdot {A_L}^2 \Big/ L_{wl} \tag{25}$$

$$\left[F_{x\_ha}, F_{x\_ha}, 0\right] = \left[F_{lon\_ha}, F_{lat\_ha}, 0\right]\cdot C_{h2i} \tag{26}$$

2.1.2. Formulating the 4-DOF balance equation

A balanced state of a sailboat satisfies multiple DOF equations. Each DOF provides an interactive interface for the subsystem forces and can reflect a coupling relationship in the sailboat system Guelfi and Canepa, 2013). For an autonomous sailing monohull, the pitch and heave balance can be neglected to balance complexity and precision since the small thrust-to-weight ratio produces little hydrodynamic lift. Eqs. (27)–(30) give the four-DOF balance equations (Fig. 6). The CE and CER are usually located at 25% of the leading edge's chord length. The centre of lateral resistance is determined from Eliasson et al. (2014), the action point of the hull aerodynamics is simplified to be the CG, and the stability arm $GZ = f(mass, CG, hull\ line)$ can be obtained by hydrostatic code.

$$F_x = F_{x\_hk} + F_{x\_s} + F_{x\_r} + F_{x\_ha} = 0 \tag{27}$$

$$F_y = F_{y\_hk} + F_{y\_s} + F_{y\_r} + F_{y\_ha} = 0 \tag{28}$$

$$M_x = F_{lat\_hk}\cdot z_{CLR} + F_{lat\_s}\cdot z_{CE} + F_{lat\_r}\cdot z_{CER} + M_{\_ha} + \Delta\cdot GZ = 0 \tag{29}$$

$$M_z = F_{lat\_hk}\cdot cos(\theta)\cdot x_{CLR} + F_{lat\_s}\cdot cos(\theta)\cdot x_{CE} + F_{lat\_r}\cdot cos(\theta)\cdot x_{CER} = 0 \tag{30}$$

2.2. Solving the balance equations

The task of the solver is to find an equilibrium that maximizes the speed under the specific external conditions, as Eq. (31).

$$(v_s, \lambda, \theta, \beta_s, \beta_r) = \underset{v_s,\lambda,\theta,\beta_s,\beta_r}{\operatorname{argmax}} v_s \mathbf{s.t.} \begin{cases} F_x &= 0 \\ F_y &= 0 \\ M_x &= 0 \\ M_z &= 0 \end{cases} \tag{31}$$

The gradient-based balance solver tends to fall into local extrema without high-quality prior performance estimation for such a high-dimensional nonconvex problem. Thus, an enhanced GA solver is adopted to solve the optimization problem with fitness $F(x)$:

$$\underset{x}{\operatorname{argmin}}\ F(x) = g(x) + f(x) \tag{32}$$

where $x = (v_s, \lambda, \theta, \beta_s, \beta_r)$, $g(x) = -v_s$, $f(x) = p\cdot\sum_{j=1}^{m} e_j^{k_j}(x)$, e_j is the error in the j^{th} constraint and k_j is the penalty parameter. The correction factor p ensures the sensitivity of $f(x)$ during the optimization process.

2.2.1. Solving states independently with the enhanced GA solver

In this optimization problem, it is a strong constraint to satisfy the multiple DOF balance equations ($f(x) = 0$), although in practice, "balance" is usually relaxed to a given tolerance ($f(x) < \varepsilon$). For any speed, the existence of equilibrium cannot be guaranteed. Therefore,

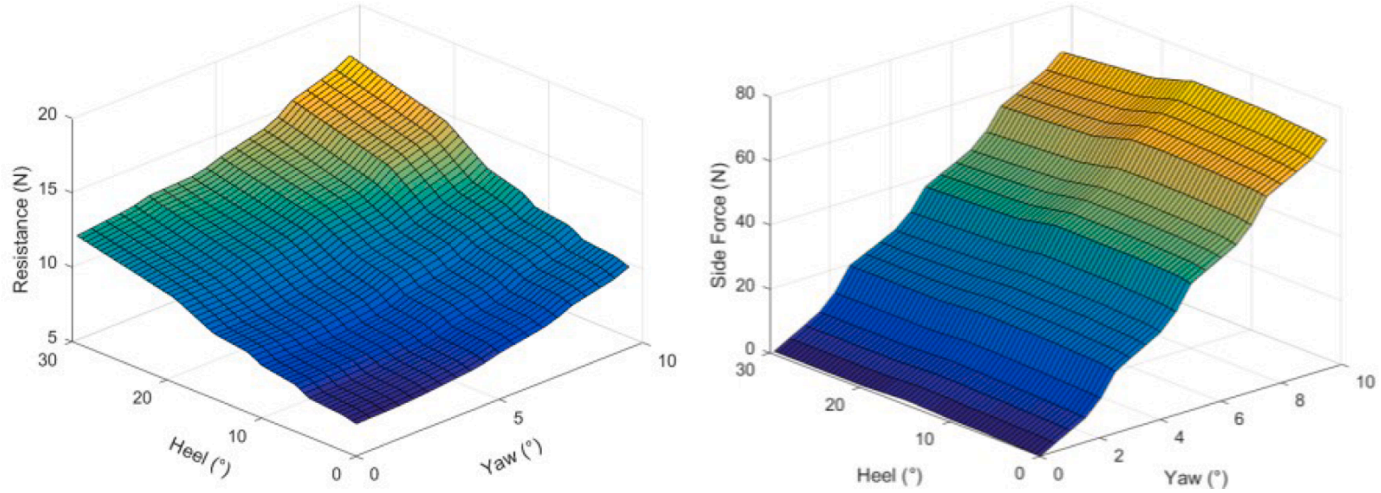

Fig. 13. Response surface for hydrodynamic forces along the X- and Y-directions at Fr=0.18.

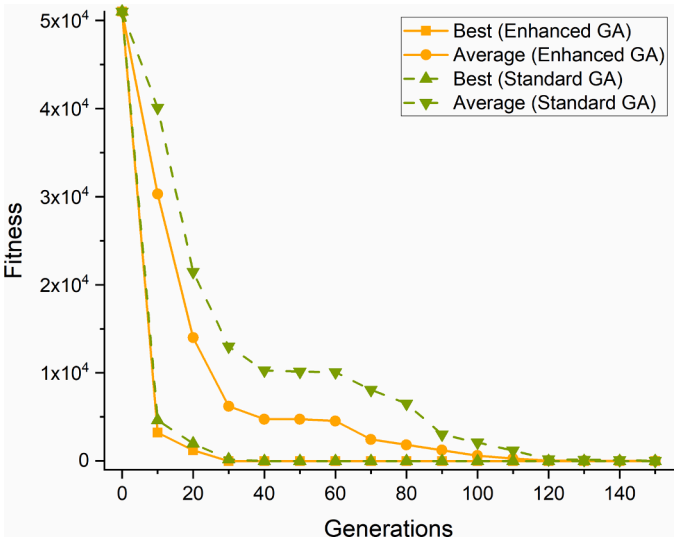

Fig. 14. Comparison of convergence rates between standard and enhanced GA solvers (the average of ten trials).

convergence (finding a good enough solution) is more important when solving a given state without prior performance estimation. For VPPs, an interesting fact is that the speed v_s is the state variable as well as a part of the fitness (Guelfi and Canepa, 2013) (Eq. (32)); when $f(x)$ is obtained, the corresponding $F(x)$ can also be obtained. Thus, we proposed an end-place enhancement GA solver to improve its convergence rate (Fig. 7). In the optimization with fitness$F(x)$, we periodically optimize 20% of the worst individuals with fitness$f(x)$. Which means replace these individuals with a more balanced state at the current speed to enhance local convergence. Once the newly obtained individual state satisfies the "balance" defined by ε (which means the solver finds a good enough solution at the currentv_s), $v_s$is recorded and used to compress the search space of the next generations (the goal is to maximize v_s). The frequency of periodic triggering of local optimization (with$f(x)$as fitness) is recommended to be once every 3–5 iterations of global optimization (with$f(x)$as the fitness), or the frequency increases with the optimization process. Premature and excessive convergence enhancement can severely weaken the global search capability.

2.2.2. *Solving adjacent states with the NIBO strategy*

Existing VPPs stop the solution process after solving each given state (one true wind speed and one true wind angle) independently. However, Guelfi and Canepa (2013) pointed out that it is almost impossible for solvers to achieve enough global searching ability for such a high-dimensional nonconvex problem. As Fig. 8 shows, insufficient global searching ability leads to fluctuations in the prediction results. However, there should be a smooth trend amongst the continuous states.

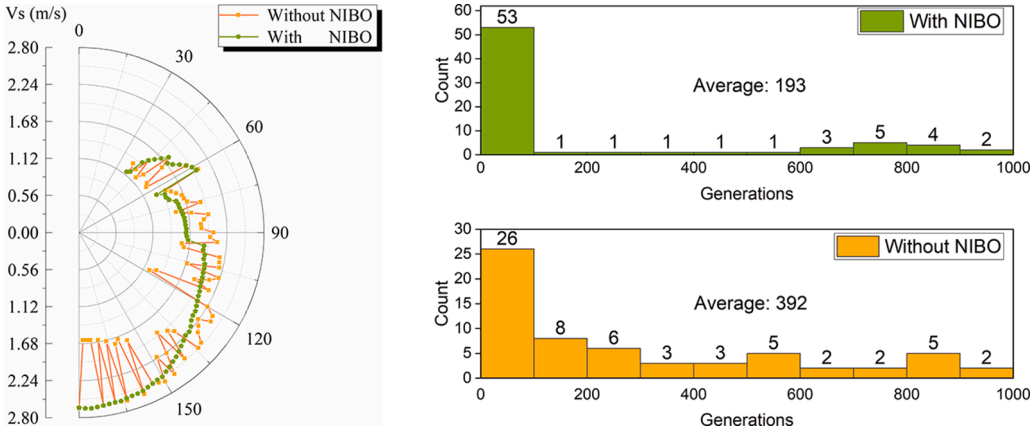

Fig. 15. The effectiveness of the NIBO strategy.

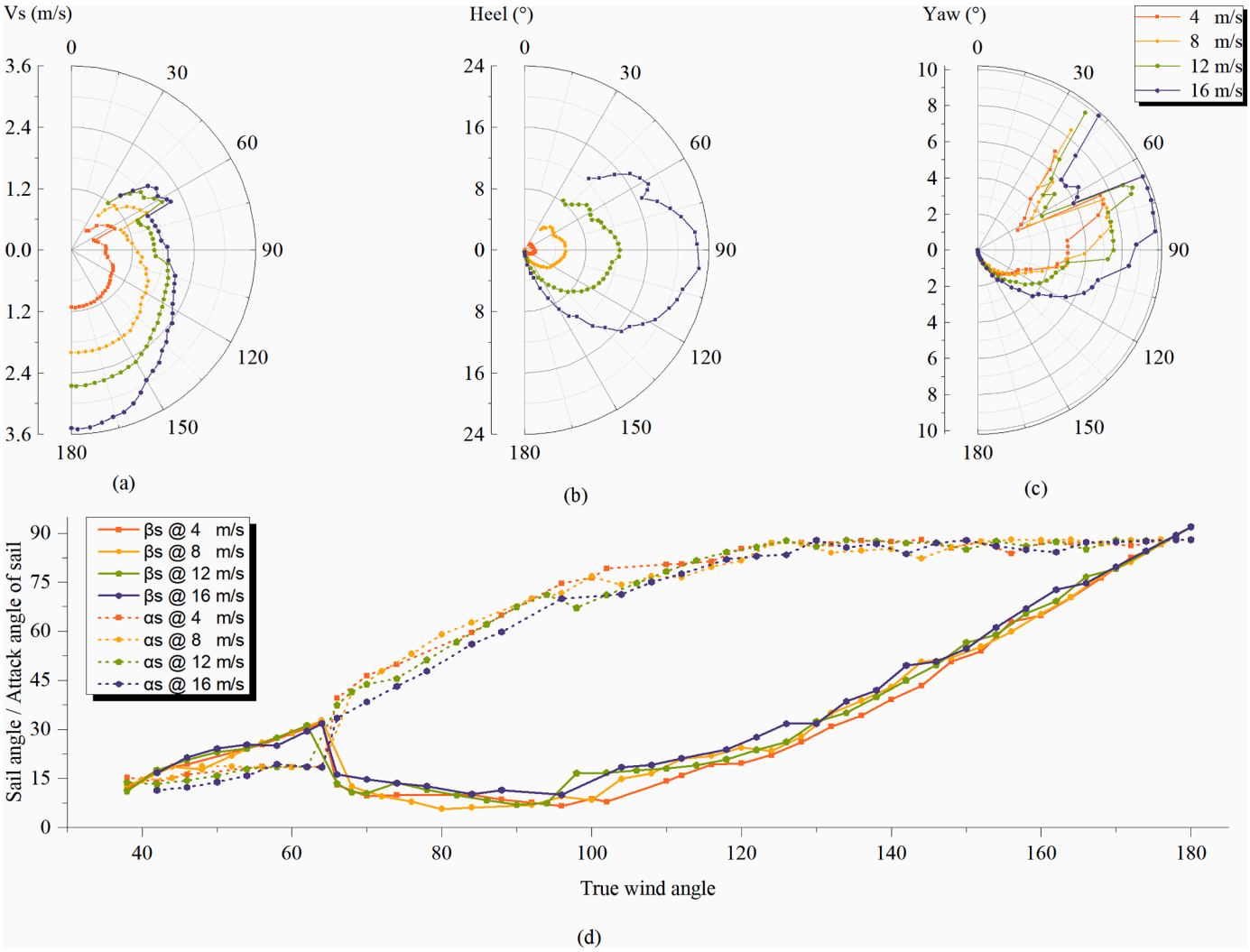

Fig. 16. VPP prediction results.

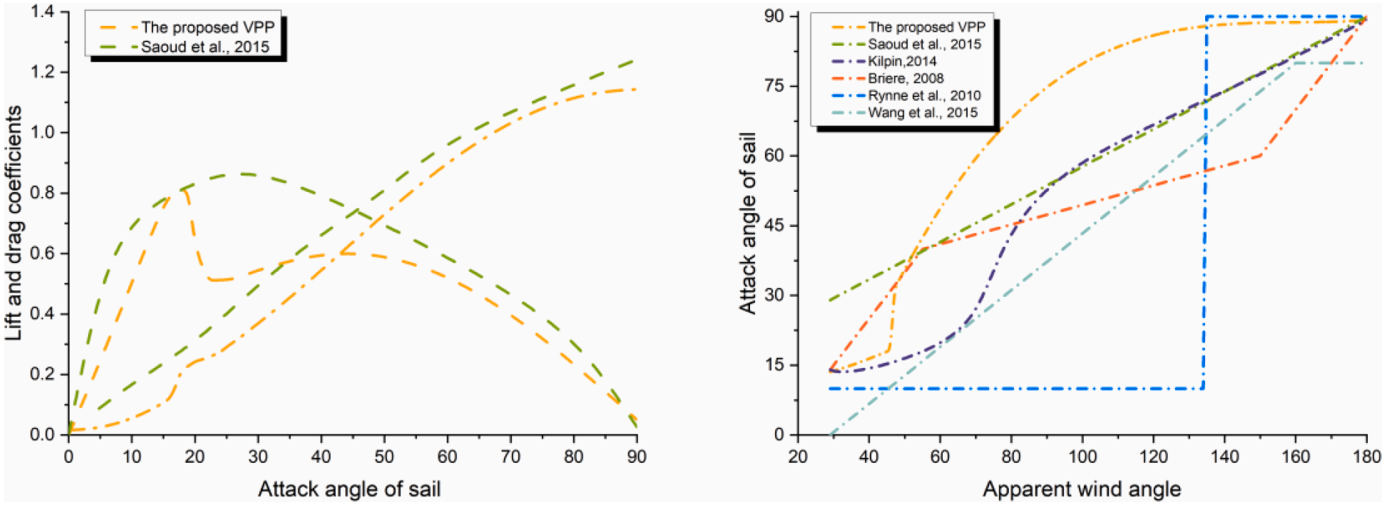

Fig. 17. Comparison of optimal sail control strategies.

The standard postprocessing method is averaging or smoothing by fitting after repeated calculation. The former will significantly increase the operation cost, and the value obtained by the latter is not the exact value obtained by the solver; that is, numerical pollution is introduced.

For our proposed VPP, the convergence is enhanced by using the end-place enhancement GA solver in the solution of the independent states, which, on the other hand, weakens the global search capability.

Therefore, we propose the NIBO strategy, which uses adjacent states'

Fig. 18. "Seagull" in preparation for her maiden voyage.

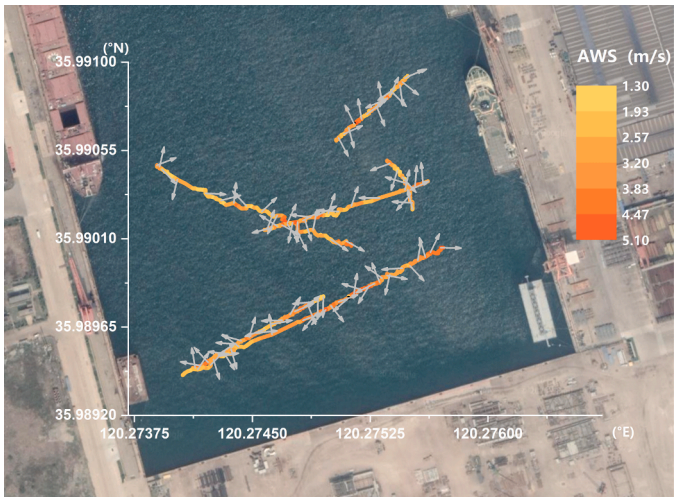

Fig. 19. Data recorded during directional navigation.

natural continuity to accelerate convergence and refine the results (Fig. 9). For any unsolved states, adjacent states are defined as states with the same TWS or TWA. The natural continuity between adjacent states is intuitive: For states with the same TWA, the speed should be faster, and the roll and yaw should be more significant in a stronger wind. For states with the same TWS, the performance is expected to be smooth rather than fluctuate. Therefore, the solved states can provide a reference for adjacent states. For states with the same TWA, individuals are more likely to fall into the range limited by neighbourhood information in the initial population generation and mutation module. Thus, the search direction is effectively guided, and the time cost is reduced. For states with the same TWS, rolling optimization is executed with the search space adjusted according to the neighbourhood information. The original solution is replaced only if the fitness of the subsequent optimization is better. The refined result is obtained when the intergenerational fitness change is negligible or the predetermined number of optimizations is achieved. The NIBO strategy makes full use of the natural continuity of adjacent states to accelerate the solution and improve the global search capability of the VPP without introducing numerical pollution.

3. Numerical and experimental verification

The proposed VPP was applied to our autonomous sailboat prototype, "Seagull." We aim to obtain performance predictions and verify the availability of the VPP. To facilitate transfer by a standard van, the overall length of the prototype is 3.42 m. The deck is designed to be flat to accommodate solar panels. The sail is designed to be rectangular and rigidly connected to the mast, rotating arbitrarily for machining convenience. A fin keel with a sweep angle is used to avoid entanglement by weeds or trash. Detailed design variables are shown in Table 2.

3.1. Acquisition of the stability curve and the aerodynamic and hydrodynamic models

The stability curve $GZ = f(mass, CG, \ hull\ line)$ of the prototype is obtained from a hydrostatic calculation code. The hydrodynamic model of the hull and keel is obtained by interpolating the CFD simulation results. Without prior performance estimation, the attack angle is restricted within [0, 95] degrees in the CFD simulations of the sail. This range is essential for the calculation because a wing sail can provide a driving force under a poststall condition. For the hull and keel, the ranges of variables are $v_s \in [0, 3.39]$ m/s, which corresponds to $Fr \in [0.05, 0.65]$. The heel angle is limited to $\theta \in [0, 30]$ degrees to maintain the deck away from the water surface. The λ value is set to $\lambda \in [0, 10]$ degrees to maintain the keel (NACA 63,015 profile) in the prestall state. The influence of the rudder angle is ignored to reduce the dimension of the matrix; thus, β_r is fixed to zero.

As illustrated in Fig. 10, left, the computational domain for the flow around the sail was block-shaped, with a width of 40 times and 20 times the chord length, and a height of 30 times the chord length. The mesh surrounding the sails is shown in Fig. 11, left. There were coarse structured cells in the exterior subdomain and finely structured cells in the subdomain around the sails. In total, 2.8 million cells are used. The front boundary is set up as a velocity inlet, the back as a pressure outlet, and the perimeter as smooth walls. At a wind speed of 5 m/s, the wind incidence at the sail was set at angles from 0 to 95 every 2 °. The range is essential for wing sails to also provide a driving force in poststall conditions. The results are arranged in the form of CL and CD, as shown in Fig. 12.

For the flow around the hull, the total domain size was $10 \times 10 \times 20$ times L_{pp}(Fig. 10, right). To capture the free surface exactly, fine cells were focused on the free surface. The boundary surface's input conditions were the inflow's speed. In total, a 3.7 million-cell mesh was employed (Fig. 11, right). The hull and keel are placed according to the corresponding attitude and draft. The force in the inertial frame, on the other hand, was the output. In total, 150 sets of CFD simulation results are interpolated to obtain response surfaces. Fig. 13 shows the response surface at Fr = 0.18.

3.2. Verification of the end-place enhancement GA solver

The specific external condition $v_t = 12m/s, \beta_t = 120^{\circ}$ is set as the test instance to verify the effectiveness of the end-place enhancement GA solver in accelerating convergence. Both enhanced and standard GA solvers are applied to find the balance ten times. The population size is 50 for the enhanced GA solver and 60 for the standard GA solver. The population setting ensures that the number of calculations of the standard solver in each generation is not less than that of the enhanced solver (the enhanced solver implements a local optimization step on 20% of the worst individuals). The results (Fig. 14) show that the end-place enhancement GA solver can effectively accelerate convergence.

3.3. Verification of the NIBO strategy

To assess the effectiveness of the NIBO strategy in terms of adjacent states of the same TWS, states of $v_t = 12m/s$ and $\beta_t \in [40^{\circ}, 180^{\circ}]$ are set as the test instances. In Case 1, the standard GA solver solves each state independently with 120 populations. Moreover, in Case 2, states are solved independently first, then 2 rounds of refinement with the NIBO strategy are adopted, and the population size is set to 40. The population

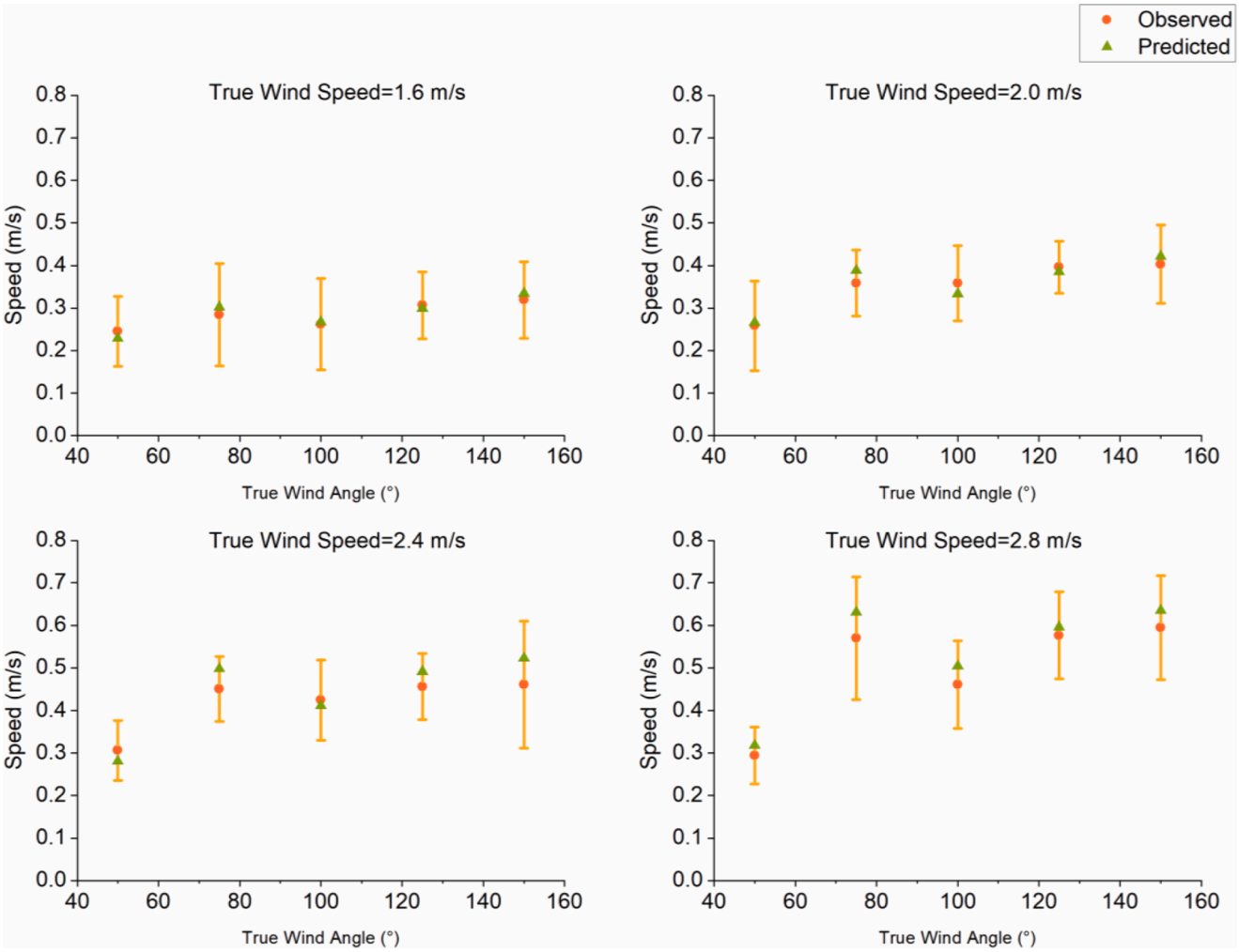

Fig. 20. Comparison of recorded data and predictions.

setting ensures that the total number of calculations of Case 1 is not less than that of Case 2. The resulting average fitness values are −7.03 and −7.77 (the smaller the cost function is, the better the result). The results (Fig. 15, left) show that the NIBO strategy can significantly improve the solver's global searching ability with lower computational costs. For adjacent states of the same TWA, states of $v_s = 8m/s$ are solved with and without the neighbourhood information of $v_s = 12m/s$. The generations required for the population's average fitness to converge to 95% of the prediction result (Fig. 15, right) show that with only one side of the neighbourhood information, the NIBO strategy can significantly accelerate the convergence.

3.4. Verification of the prediction result

3.4.1. Numerical verification

As a result of the prediction, the maximum speed and the corresponding attitude are shown in Fig. 16a–c. The optimum sail trimming is shown in Fig. 16d. No feasible solution is found for $\beta_t \in [0,\ 38]$ degrees at all v_t, which can be interpreted as a 'no-go zone' for the prototype. For upwind conditions, a step is observed for a β_t of approximately 65 °, and steps in α_s are observed from 19 ° to approximately 35 ° (Fig. 16a, b, and d). To explain these steps, we compared our results with those of Saoud et al. (2015). The optimal sail trimming of an autonomous sailboat robot with a flat sail and the sail characteristics in lift and drag coefficient curves are available in the literature. The comparative analysis in Fig. 17 shows that the unusual step comes from the step in the characteristic wing sail curves near the stall angle.

The optimization results of the proposed VPP indicate that for the case of zero β_r, the sail functions in the prestall state only when β_t is below a small angle (65 ° in this case) but functions in the poststall state most of the time. When β_s is greater than 140 °, the sail is almost perpendicular to the wind, similar to a spinnaker (Fig. 17, right). The results are verified via comparison with the literature. Tretow (2017) reported that for optimal sail trimming of a free rotating wing sail, α_s should be maintained at 12 ° for all apparent wind angles (AWAs) because 12 ° provides the maximum lift-to-drag ratio of the wing. However, this strategy is unreasonable for a directly controlled wing sail because the drag when sailing downwind can provide a driving force for a sailboat. Similar strategies have been reported by other researchers (Briere, 2008; Rynne and von Ellenrieder, 2010; Wang et al., 2015): a small α_s with a large lift-drag ratio is adopted for a sail under upwind conditions, which then somehow undergoes a transition to becoming completely perpendicular to the wind at 180 ° for all AWAs (in Wang et al. 2015, the authors stated that 80 ° is the upper limit of β_s for their sailboat). Considering fixed α_s under upwind conditions, as in Rynne and von Ellenrieder (2010), we do not obtain a solution that satisfies the four-DOF constraint. In conclusion, the predictions may appear anomalous, but the authors consider the results are credible and applicable.

3.4.2. Experimental verification

Directional navigation tests are adopted to validate the effectiveness of the VPP. The sea trial was performed at pier 8 of the Qingdao Beihai

Shipbuilding Heavy Industry Co., Ltd., site in October 2019 (Fig. 18). Due to the lifting of safety regulations of the shipyard, the sea trial was only allowed in the breeze. During tests, the prototype is asked to navigate along a straight trajectory. The following quantities were recorded with timestamps at approximately 1 s intervals: The track, apparent wind speed, and apparent wind angle were determined from a weather station mounted on the bow. The weather station has a 3 m accuracy in GPS position and a 5% error in apparent wind speed with 0.1 m/s resolution. For the apparent wind direction, the accuracy is $\pm 3^\circ$ with a resolution of 0.1°. The steering angle of the sail is set as a specific function of the apparent wind angle (of the inertial frame). The rudder angle depends on the heading control algorithm. Both measurements were performed with a rotary potentiometer. There was a gap in the gear meshing of the prototype's rotating sail mechanism, and there was a total error of $\pm 3.0^\circ$ between the actual sail angle and the recorded value. We are unable to provide data on the current, but the water surface appeared calm. According to the safety rules of the shipyard, an auxiliary boat must be followed during trials. Therefore, we devoted our best efforts to ensuring that the boat was positioned far enough from the prototype. Data are shown in Fig. 19. The apparent wind speeds (AWSs) are colour-coded along the track, and some apparent wind angles are expressed as vectors.

In such a semienclosed region, wind conditions change frequently. We check whether the segment between T_{x-10} and T_{x+10} (approximately 20 s) satisfies the apparent wind speed change within 0.4 m/s and the apparent wind angle within 20° for each time point T_x. For the segments that meet the conditions, we obtain the corresponding average speed, average apparent wind speed and angle (of the inertial frame); furthermore, the average true wind speed and angle can be derived (speed, true wind, and apparent wind form a vector triangle). Then, we group part of the data with true wind speeds of 1.6, 2.0, 2.4, and 2.8 m/s $\pm$ 0.2 m/s and true wind angles of 50, 75, 100, 125, and $150^\circ \pm 5^\circ$. The average speed and standard deviation of each group were counted. For comparison, the representative value of each group (1.6 m/s 50°, 2.4 m/s 150°, etc.) and the corresponding sail angle (the same function as the controller) are introduced into the VPP to obtain the prediction.

The comparison of recorded data and predictions is shown in Fig. 20. We consider that the relatively large variance of the observations is due to the slight wind during the sea trial, wind changes, and systematic errors in observations. However, if the wind is strong, for such a semienclosed region, the waves and currents accompanying the wind will act on the platform through complex reflections, and it is also difficult to guarantee that better results will be adopted. As the wind increases, the trend of VPP overestimating the speed increases. This may be because the weather station is lower than the aerodynamic centre of the sail (considering the presence of wind gradients). Other possible sources of error include that VPP does not consider wave-added resistance models and inaccuracies in subsystems' aerodynamic and hydrodynamic models. However, most importantly, the overall trend of the predictions with the sea trial data confirms the validity of the proposed VPP. The proposed VPP can qualitatively evaluate an autonomous sailing monohull design considering the predicted speed as a design score.

4. Conclusions and future studies

This paper's main contribution is developing a generalized VPP for autonomous sailing monohulls. Designers can effectively evaluate their designs with subsystem aerodynamic and hydrodynamic models from any source, especially in the early stages. Considering that the prior performance estimation is difficult to obtain, we provide solutions at two levels. First, we design a GA solver with an end-place enhancement module, accelerating convergence when solving independent external conditions. Then, we proposed an NIBO strategy that can accelerate and refine solutions with the relationship between adjacent external conditions. We apply the proposed VPP to our prototype design and verify the effectiveness of the enhanced GA solver and NIBO strategy. A comparison of data from the literature and sea trial data indicates that the predicted results of the proposed VPP are effective and interpretable. Therefore, the proposed VPP can serve as a powerful tool for further design optimization of autonomous sailing monohulls.

A limitation of the proposed VPP is the absence of a wave-added resistance model, which may result in performance prediction errors for practical oceanic applications. A wave-added resistance model will be added in future studies, and additional sea trials will be conducted to calibrate the VPP. A design of experiment (DOE) strategy will be developed to obtain the hull and keel hydrodynamics model because CFD computation is the most time-consuming component in practice.

CRediT authorship contribution statement

Yang An: Conceptualization, Methodology, Software, Writing – original draft, Investigation, Visualization. **Jiancheng Yu:** Conceptualization, Resources, Supervision, Project administration, Writing – review & editing. **Feng Hu:** Methodology, Software. **Zhenyu Wang:** Methodology, Writing – review & editing.

Declaration of Competing Interest

The authors declare that they have no known competing financial interests or personal relationships that could appear to influence the work reported in this paper.

Acknowledgments

This work was supported in part by the National Natural Science Foundation of China (Grant No. 51909257), Natural Science Foundation of Liaoning Province, China (Grant No. 2021-MS-031), Doctoral Scientific Research Foundation of Liaoning Province (Geant No.2021-BS-019) and in part by the State Key Laboratory of Robotics at Shenyang Institute of Automation, China (Grant No. 2020-Z06). Our deepest gratitude goes to the anonymous reviewers for their thoughtful suggestions that have helped improve this paper substantially. We are grateful to Jianwei Huang and Jie Liu for providing clear illustrations. We would like to thank Jin Zhang, Shuai Kang, Tianzhu Gao, Dr. Lin Du (NBU) and Hongshen Xu (OUC) for critically reading our manuscript.

References

Abbott, I.H., Von Doenhoff, A.E., 2012. Theory of Wing Sections: Including a Summary of Airfoil Data. Courier Corporation.

An, Y., Yu, J., Zhang, J., 2021. Autonomous sailboat design: a review from the performance perspective. Ocean Eng. 238, 109753 https://doi.org/10.1016/j.oceaneng.2021.109753.

Augenstein, T., Singh, A., Miller, J., Pomerenk, A., Dean, A., Ruina, A., 2016. Using a controlled sail and tail to steer an autonomous sailboat. In: Proceedings of the World Robotic Sailing Championship and International Robotic Sailing Conference, pp. 91–103. Springer.

Baker, R., Kambourian, L., Hajarian, S., Augenstein, T., Harnett, S., Lee, G.-M., Sudarshan, M., Richter, C., Trouillot, C., Williamson, P., others, 2015. Design and development of a self-stabilizing, autonomous sailboat with zero-net stored-energy use. In: Proceedings of the World Robotic Sailing Championship and International Robotic Sailing Conference, pp. 39–57. Springer.

Briere, Y., 2008. Iboat: an autonomous robot for long-term offshore operation. In: Proceedings of the MELECON the 14th IEEE Mediterranean Electrotechnical Conference, pp. 323–329. IEEE.

Clark, N.A., Validation of a sailing simulator using full scale experimental data, PhD Thesis, University of Tasmania, 2014.

De Robertis, A., Lawrence-Slavas, N., Jenkins, R., Wangen, I., Mordy, C.W., Meinig, C., Levine, M., Peacock, D., Tabisola, H., 2019. Long-term measurements of fish backscatter from Saildrone unmanned surface vehicles and comparison with observations from a noise-reduced research vessel. ICES J. Mar. Sci.

Domínguez-Brito, A.C., Valle-Fernández, B., Cabrera-Gámez, J., Ramos-de-Miguel, A., García, J.C., Friebe, A., Haug, F., 2016. A-TIRMA G2: an Oceanic Autonomous Sailboat. Robotic Sailing 2015. Springer International Publishing, Cham, pp. 3–13. http://link.springer.com/10.1007/978-3-319-23335-2_1 (accessed May 9, 2020).

Eliasson, R., Larsson, L., Orych, M., 2014. Principles of Yacht Design. A&C Black.

Fossati, F., Muggiasca, S., Viola, I.M., Nov, 2006. An investigation of aerodynamic force modelling for IMS Rule using wind tunnel techniques. In: Proceedings of the 19th

HISWA Symposium on Yacht Design and Yacht Construction. Amsterdam, The Netherlands, pp. 13–14.
Fujiwara, T., Ueno, M., Nimura, T., 1998. Estimation of wind forces and moments acting on ships. J. Soc. Naval Arch. Jpn. 1998, 77–90.
Gerritsma, J., 1968. Course keeping qualities and motions in waves of a sailing yacht. Faculty of Marine Technology, Ship Hydromechanics Laboratory, Report No. 200-P. In: Proceedings of the 3rd AIAA Symposium Aero, Hydronautics of Sailing. TU Delft.
Gormand, M., Full Scale Test Case For Sailing Yacht Performance, (2015).
Graf, K., Bohm, C., 2005. A new velocity prediction method for post-processing of towing tank test results. In: Proceedings of the 17th Chesapeake Sailing Yacht Symposium.
Guelfi, G., Canepa, E., New development in 6-Dof algorithms for sailing Yacht velocity prediction program and new insight in appendages force modelling, University of Genoa, Italy (2013).
Jackson, P., 1996. Modelling the aerodynamics of upwind sails. J. Wind Eng. Ind. Aerodyn. 63, 17–34.
Jackson, P.S., 2001. An improved upwind sail model for VPPs. In: Proceedings of the SNAME 15th CSYS.
de Jong, P., Katgert, M., Keuning, L., 2008. The development of a velocity prediction program for traditional Dutch sailing vessels of the type Skûtsje. In: Proceedings of the 20th HISWA Symposium.
Kerwin, J., A velocity prediction program for ocean racing yachts. The Society of Naval Architects and Marine Engineers, SNAME, Report 75-17 Massachusetts Institute of Technology, MIT, Department of Ocean Engineering, Ocean Race Handicapping Project (1975).
Keuning, J., Sonnenberg, U.B., Approximation of the hydrodynamic forces on a sailing yacht based on the'Delft Systematic Yacht Hull Series', 15th International symposium on Yacht Design and Yacht Construction, Amsterdam, 16 November 1998: proceedings, WbMT, 99–152, 1998.
Keuning, J., Katgert, M., Vermeulen, K.J., 2006. Keel-rudder interaction on a sailing yacht. In: Proceedings of the 19th International HISWA Symposium on Yacht Design and Yacht Construction. Amsterdam, The Netherlands.
Klinck, H., Fregosi, S., Matsumoto, H., Turpin, A., Mellinger, D.K., Erofeev, A., Barth, J. A., Shearman, R.K., Jafarmadar, K., Stelzer, R., Friebe, A., Haug, F., 2016. Mobile autonomous platforms for passive-acoustic monitoring of high-frequency cetaceans. Robotic Sailing 2015. Springer International Publishing, Cham, pp. 29–37. http://link.springer.com/10.1007/978-3-319-23335-2_3. accessed May 19, 2020.
Lasher, W.C., Sonnenmeier, J.R., Forsman, D.R., Zhang, C., White, K., 2003. Experimental force coefficients for a parametric series of spinnakers. In: Proceedings of the SNAME 16th Chesapeake Sailing Yacht Symposium. OnePetro.
Martin, D., Beck, R.F., Pcsail, a velocity prediction program for a home computer, in: SNAME 15th Chesapeake Sailing Yacht Symposium, OnePetro 2001.
Meinig, C., Lawrence-Slavas, N., Jenkins, R., Tabisola, H.M., 2015. The use of Saildrones to examine spring conditions in the Bering Sea: vehicle specification and mission performance. In: Proceedings of the Oceans 2015-MTS/IEEE Washington, pp. 1–6. IEEE.
Miller, P., Judge, C., Sewell, D., Williamson, S., 2018. An alternative wing sail concept for small autonomous sailing craft. Robotic Sailing 2017. Springer, pp. 3–17.
Neal, M., 2006. A hardware proof of concept of a sailing robot for ocean observation. IEEE J. Ocean. Eng. 31, 462–469.
ORC VPP - Designer's version, (2020). https://orc.org/index.asp?id=41.
Rynne, P.F., von Ellenrieder, K.D., 2010. Development and preliminary experimental validation of a wind-and solar-powered autonomous surface vehicle. IEEE J. Oceanic Eng. 35, 971–983.
Saoud, H., Hua, M.D., Plumet, F., Amar, F.Ben, 2015. Optimal sail angle computation for an autonomous sailboat robot. In: Proceedings of the 54th IEEE Conference on Decision and Control (CDC). Osaka, pp. 807–813. https://doi.org/10.1109/CDC.2015.7402329. IEEE.
Silva, M.F., Friebe, A., Malheiro, B., Guedes, P., Ferreira, P., Waller, M., 2019. Rigid wing sailboats: a state of the art survey. Ocean Eng. 187, 106150.
Tretow, C., Design of a free-rotating wing sail for an autonomous sailboat, 2017.
Wang, Q., Kang, M., Xu, J., Xu, J., 2015. Autonomous sailboat track following control. In: Proceedings of the World Robotic Sailing Championship and International Robotic Sailing Conference, pp. 125–136. Springer.
Whicker, L.F., Fehlner, L.F., Free-stream characteristics of a family of low-aspect-ratio, all-movable control surfaces for application to ship design, David Taylor Model Basin Washington DC, 1958.